Volume 1 | Number 1 | Jan 2013 | Pages 1–100

Nanoscale

www.rsc.org/nanoscale

ROYAL SOCIETY OF CHEMISTRY

www.rsc.org/nanoscale

Confinement Induced Ordering in Dewetting of Ultra Thin Polymer Bilayers on Nano Patterned Substrates

Nandini Bhandaru, Anuja Das, and Rabibrata Mukherjee[*]

Instability and Soft Patterning Laboratory, Department of Chemical Engineering
Indian Institute of Technology Kharagpur, West Bengal, Pin 721302, India

*Author to whom correspondences should be addressed. Tel: +91–3222 283912, e–mail: rabibrata@che.iitkgp.ernet.in

Abstract

We report dewetting of a thin bilayer of Polystyrene (PS) and Poly(methylmethacrylate) (PMMA) on a topographically patterned non wettable substrate comprising array of pillars, arranged in a square lattice. With gradual increase in the concentration of PMMA solution (C_{n-PMMA}), the morphology of the bottom layer changes as: 1) aligned array of spin dewetted droplets arranged along substrate grooves at very low C_{n-PMMA}; 2) interconnected network of threads surrounding each pillar at intermediate C_{n-PMMA}; and 3) continuous bottom layer at higher C_{n-PMMA}. On the other hand the morphology of the PS top layer depends largely on the nature of the pre-existing bottom layer, in addition to C_{n-PS}. An ordered array of PMMA core – PS shell droplets forms right after spin coating when both C_{n-PMMA} and C_{n-PS} are very low. Bilayers with all other initial configurations evolve during thermal annealing, resulting in variety of ordered structures. Unique morphologies realized include laterally coexisting structures of the two polymers confined within the substrate grooves due to initial rupture of the bottom layer on the substrate followed by a squeezing flow of the top layer; an array of core-shell and single polymer droplets arranged in an alternating order etc. to highlight a few. Such structures cannot be fabricated by any stand alone lithography technique. On the other hand, in some cases the partially dewetted bottom layer imparts stability to an intact top PS layer against dewetting. Apart from ordering, under certain specific conditions significant miniaturization and downsizing of dewetted feature periodicity and dimension as compared to dewetting of a single layer on a flat substrate is observed. With the help of a morphology phase diagram we show that ordering is achieved over a wide combination of C_{n-PMMA} and C_{n-PS}, though the morphology and dewetting pathway differs significantly with variation in the thickness of the individual layers.

Introduction

Thin polymer films on solid surfaces find important applications in coatings, adhesives, biological membranes, fabrication of nonlinear optical devices, sensors, organic photovoltaic, etc. However, due to various inter molecular interactions at the meso scale, long term stability of such films is often a matter of concern.[1–12] For example, an ultra thin film (thickness, $h < 100$ nm) when thermally annealed above the glass transition temperature (T_G) of the constituent polymer or exposed to solvent vapor may spontaneously rupture and subsequently dewet on a non wettable substrate, which is both scientifically intriguing and practically important.[1–12] Films thinner than $h \approx 10$ nm rupture due to amplification of thermally excited capillary waves following the spinodal mechanism.[1–3] Slightly thicker films with h in the range of 10 to 100 nm rupture due to nucleation of holes around substrate heterogeneities.[4–12] The ruptured holes subsequently grow, coalesce, and eventually result in an array of nearly equal sized but random dewetted droplets, the periodicity (λ_D) and size (d_D) of which depends on the initial h. While such instability is undesirable from the standpoint of thin coatings,[13–15] morphological self organization during dewetting can be a potential technique for engineering meso scale features with the ability of morphology control.[6]

In contrast to the single film scenario, dewetting of an ultra thin polymer bilayer is a more fascinating and complex problem offering richer physics due to simultaneous and coupled deformation of the film – air and the film – film interfaces.[16–46]. In a thin bilayer, depending on the nature of the coupling of the deformable interfaces, rupture can occur via two distinct instability modes.[17–19] Bending mode is observed when the deformation of the two interfaces are in phase and typically leads to preferential rupture of the bottom layer under an intact top layer. In contrast, in squeezing mode the deformation of the two coupled interfaces are out of phase and results in the rupture of the top layer over an intact bottom layer.[19] Based on experiments,[22–

[46] as well as full nonlinear simulations,[18–21] it has been shown that a myriad of submerged, embedded, encapsulated, hollow or core-shell type meso-scale structures can result from dewetting of a thin polymer bilayer. Several recent experimental studies have also focussed on how a change in the dewetting mode can occur as a function of film properties such as thickness or viscosity of the constituent layers.[35,41] Dewetting of a thin polymer bilayer has been utilized in patterning of protein molecules,[45] and water harvesting from mist.[46] Reduced interfacial tension at the polymer – polymer interface also leads to downsizing of the dewetted structures.

Despite the ease of fabrication and high degree of flexibility in morphology control, the practical utility of instability mediated patterning approaches is limited as they produce inherently random structures. This limitation is overcome by combining the essential concepts of top down and bottom up fabrication approaches, that is by dewetting the film either on a chemically,[47–56] or a topographically patterned substrate.[57–68] This has been thoroughly investigated both experimentally,[51–68] and based on 3-D numerical simulations.[47–50] A variety of ordered or partially disordered structures result depending on the commensuration of the substrate pattern periodicity (λ_P) and the wavelength of instability corresponding to the initial thickness of the film (λ_D).[47–52,56] On a chemically patterned substrate, dewetting is engendered by an in-plane potential gradient, which causes flow of liquid from the less wettable to the more wettable areas, leading to rupture of the film over the less wettable domains.[47,48,52] In contrast, periodic variation in film thickness on a topographically patterned substrate favours rupture of the film over the thinnest areas thereby imposing directionality to the evolving structures.[67,68] A recent work reported the alignment of polymer nano droplets on a flat template free substrate by dewetting of a pre-patterned film, if the film ruptures at the thinnest locations ahead of surface tension induced flattening.[70]

Surprisingly, ordering of the structures resulting from dewetting of a thin polymer bilayer on a patterned substrate has received far less attention in comparison to its single film counterpart, probably because of the experimental complexities involved and complex multi parameter nature of the problem. Based on long wave nonlinear 3-D numerical simulations, Sharma and co-workers predicted the evolution pathway and final dewetted morphology of a bilayer on both topographically and chemically patterned substrates.[71,72] Their simulations show that the relative magnitudes of surface tension of the two layers and the substrate, vis–a–vis the spreading coefficients between different components result in clearly distinct evolution routes and final morphologies.[71] Recently, Ding and co-workers reported the thermal dewetting of a nano imprinted bilayer,[73] and a bilayer with a corrugated interface.[74–76] They obtained partial ordering which include aligned domains orthogonal to the direction of the initial stripes as the bottom layer undergoes surface tension induced flattening prior to capillary breakup of the top layer.[74,75] Their work suggests that by suitable control of the rupture sequence in a patterned bilayer it may become possible to create myriad of hierarchical structures by adjusting the geometry and properties of the individual layers.[76] Recently, some of us reported the dewetting of a PS – PMMA bilayer on a grating patterned substrate and showed that it becomes possible to obtain an array of core–shell droplets. However, droplet formation gets suppressed in favour of undulating threads with increase in the thickness of either of the layers.[77]

It thus becomes clear that experimental studies on dewetting of a thin polymer bilayer on topographically patterned substrates with complex geometry is absent and needs further attention. In this article, we report the dewetting of a PS – PMMA bilayer on a topographically patterned substrate comprising 2–D array of square pillars (Fig. 1A) with submicron lateral dimension. The bilayers are prepared by direct sequential spin coating on the patterned substrates using mutually exclusive solvents.[77] On a topographically patterned substrate with low surface

energy (γ_{sub} less than both γ_{PMMA} and γ_{PS}), a discontinuous film forms at a low C_n due to dewetting of the solution layer during spinning itself.[67] Based on $C_{n\text{-}PMMA}$, we identify three different morphology regimes for the bottom PMMA layer. **Type 1** morphology comprises of an array of aligned PMMA droplets arranged along the substrate grooves at very low $C_{n-PMMA} \leq$ 0.15% (Fig. 1B).[78] In **Type 2** morphology, interconnected network of PMMA threads fill the substrate grooves surrounding the pillars at intermediate C_{n-PMMA} varying between 0.2% and 1.5% (Fig. 1C and 1D). A **Type 3** structure refers to a continuous bottom layer for $C_{n-PMMA} >$ 2.0%. Depending on C_{n-PS}, the top PS layer can also be discontinuous (low C_{n-PS}) or continuous (high C_{n-PS}). It is observed that PS layer fully wets PMMA domains even at low C_{n-PS} and spin dewets only over the areas where the substrate is exposed. Thus for every possible morphology of the bottom PMMA layer, a discontinuous (**D**) or a continuous (**C**) top PS layer may form depending on C_{n-PS}. We use a combination of the above classifications to identify different types of bilayers in the following way: Type 1C/ 2C/ 3C bilayer implying a continuous PS film over an array of PMMA droplets, PMMA threads and a continuous a PMMA film respectively. Similarly, Type 1D/ 2D bilayer refers to a discontinuous PS layer over array of PMMA droplets and PMMA threads respectively. As PS always wets the bottom PMMA film, no bilayer with identification tag 3D is obtained.

Materials and Methods

The topographically patterned substrates were soft lithographically fabricated on 5 μm thick Sylagrad 184 (a two part cross linkable Polydimethylsiloxane (PDMS); Dow Corning, USA) films. The oligomer (part A) to cross-linker (part B) ratio was 10:1 (wt/wt). Dilute solution of Sylgard 184 in n-hexane (Merck, Germany) was spin coated on cleaned double side polished quartz pieces (15 mm ×15 mm, Applied optics, India) to obtain 5μm thick films. Flexible Sylgard 184 stamps containing negative replica of the desired patterns were used for embossing

the Sylgard 184 thin films. The as cast Sylgard 184 films were patterned using a modified pressure assisted imprinting technique which relied on capillary driven mold filling for pattern replication.[79] Details of patterning an uncross-linked Sylgard 184 film with a Sylgard 184 stamp (avoiding cohesive bonding) is available elsewhere.[79] The embossed films were cured in a vacuum oven at 120 °C for 12 hours for complete cross linking and pattern replication. The patterned Sylgard 184 films were subsequently exposed to UV−ozone treatment for 30 minutes in an UV – Ozone chamber (PSD Pro UV−O, Novascan, USA). This exposure resulted in the formation of a stiff surface oxide layer of silicon which acts as a diffusion barrier against solvent penetration into the Sylgard 184 matrix during subsequent spin coating and selective solvent washing,[80,81] which has also been verified by Roy et al.[67] The UVO exposed patterned Sylgard 184 substrates were completely wettable by the polymer solution. To make the surface non-wettable which is desirable for studying dewetting, the substrates were silanized with octadecyl-trichloro-silane (OTS, 95% pure, Aldrich, UK) by keeping them immersed in a dilute OTS solution (5 µL of OTS in a 13 ml n-hexadecane) for 1 hour. The silanized substrates after washing in water and drying were ready for use.[78] An AFM scan of the patterned substrate is shown in Fig. 1A. Both width and breadth of the pillars (L_P) is 500 nm, height (h_P) 250 nm, with a periodicity (λ_P) of 1.5 µm, and are arranged in a square lattice in both X and Y directions. Patterned Sylgard substrates were preferred as they can be easily fabricated at low cost. Similar substrates have recently been used in several dewetting related studies.[64–68,77,78]

The bilayers were prepared by sequential spin coating (Apex Instruments, India) of PMMA (MW: 350 K, Sigma, U.K.) and PS (MW: 280 K, Sigma, U.K.) from their dilute solutions in Toluene (HPLC Grade) and 1-Chloropentane (HPLC grade, Merck India) respectively. The drop volume, revolutions per minute (rpm) and spin duration for both the layers were maintained at 200 µL, 2500 rpm, and 1 minute respectively. After coating each layer, the films were annealed

in a vacuum oven at 60 °C for 3h to remove any remnant solvent. The morphology of each sample was scanned twice using an AFM (5100, Agilent Technologies) in intermittent contact mode with silicon cantilever (PPP-NCL, Nanosensors Inc, USA), once after coating the bottom layer and then again after coating the top layer. Dewetting in the samples was engendered by annealing them in an air oven at 130 °C, a temperature that is higher than the T_G of both the polymers. Samples were taken out from the oven periodically to study the morphological evolution using the AFM. For every sample, the AFM analysis was performed after every 15 min of thermal annealing for the initial 3h and thereafter it was imaged after every 1h of annealing. However in certain cases scans were performed after every 5 minutes of annealing to accurately capture morphological transitions. In these cases, an in-situ thermal stage attached to the AFM was used. Thus the maximum error in time reading is limited to ± 5 minutes. Eventually, every sample was annealed up to 24h to see if there was any late stage dynamics. To understand the morphology of the individual polymer domains, selective extraction of the phases was performed. For removing the PS domains the samples were dipped in 1–Chloropentane for 1 minute. PMMA domains were removed by UVO induced degradation instead of selective solvent wash, as acetic acid (selective solvent for PMMA) was seen to damage the Sylgard substrate due to the rather long washing time (approximately 10 minutes). After washing, the samples were dried at 60°C under vacuum for 3h for removal of any remnant solvent before scanning with the AFM. All the dewetting mechanisms are proposed based on careful analysis of the AFM phase contrast images at every step and by selective removal of each phase.

The surface energy of the substrate was calculated from Owen's equation, γ_{sub} = 24.2 mJ/m^2, using water, ethylene glycol, and toluene as probing liquids.[82] The surface energies of PS and PMMA were γ_{PS} = 38.3 mJ/m^2 and γ_{PMMA} = 41.8 mJ/m^2 respectively.[77] The equilibrium contact angles of toluene and 1–chloropentane on the patterned silanized substrates were found to be ~

35° and 32° respectively, measured using a Contact Angle Goniometer (make: Ramé-hart, USA, Model 290). This implies that the substrate was partially wetted by the solvents for both the layers. The spreading coefficients, $S_{PMMA-Sub} < 0$ as well as $S_{PS-Sub} < 0$ which suggests that both the polymers were unstable and hence dewet when in contact with the substrate.[71] The spreading coefficient, $S_{PS-PMMA} > 0$ which accounts for the preferential wetting of PS on PMMA layer. All the results are explained based on the surface energy data and spreading coefficients. As a thin film directly spin coated on a topographically patterned substrate is either discontinuous or has undulating top surface, it is difficult to define an exact thickness (h).[67,68,77] For such films, an equivalent film thickness (h_E) is typically defined which corresponds to the thickness of a film coated under identical conditions on a flat substrate of the same material.[67] The thickness of these flat films were measured using a variable angle imaging ellipsometer (Accuron GmbH, Model: EP3SW, 532 nm laser source). The effective thickness of various top (h_{E-PS}) and bottom (h_{E-PMMA}) layer films used in the present study are listed in Table 1.

Table 1: Equivalent Thickness of Films on Patterned Substrate

$c_{n\text{-}PMMA}$ (%)	$h_{E\text{-}PMMA}$ (nm)	Morphology	Type	Droplet Diameter, d_D (nm)	Droplet Height, h_D (nm)	Thread Diameter, L_T (nm)	Thread Height, h_T (nm)	Lowest Continuous Film Height, h_L (nm)	a_S (nm)	Schematic Representation of the Bottom Layer, Cross Section of the Substrate
0.1	*	Spin Dewetted Droplet	Type 1	332.1 ± 5.0	80.3 ± 3.0	--	--	--	--	
0.25	*	Discontinuous-interconnected network of threads (INT)	Type 2	--	--	358.0 ± 2.9	52.0 ± 0.9	--	--	
0.5	21.1 ± 0.3	Discontinuous-INT	Type 2	--	--	434.2 ± 5.1	68.9 ± 3.2	--	--	
0.75	28.5 ± 0.6	Discontinuous-INT	Type 2	--	--	500.0	115.1 ± 2.7	--	--	
1.0	38.9 ± 0.2	Discontinuous-INT	Type 2	--	--	500.0	188.4 ± 0.5	--	--	
1.25	53.2 ± 0.6	Discontinuous-INT	Type 2	--	--	500.0	262.1 ± 2.3	--	--	
1.5	62.6 ± 0.8	Discontinuous-INT	Type 2	--	--	500.0	294.1 ± 5.0	--	--	
2	74.0 ± 0.4	Continuous	Type 3	--	--	500.0	293.4 ± 2.2	18.0 ± 1.0	25.3 ± 0.7	
2.5	88.4 ± 0.8	Continuous	Type 3	--	--	500.0	295.5 ± 3.4	25.1 ± 1.6	20.8 ± 0.2	
$c_{n\text{-}PS}$	$h_{E\text{-}PS}$ (nm)									
0.1	*	Spin Dewetted Droplet		346.5 ± 2.0	77.2 ± 1.75	--	--	--	--	
0.25	*	Discontinuous		--	--	371.3 ± 3.1	48.8 ± 0.5	--	--	
0.5	22.3 ± 0.4	Discontinuous		--	--	426.0 ± 4.6	65.3 ± 2.7	--	--	
1.0	41.8 ± 0.7	Discontinuous		--	--	500.0	183.7 ± 1.8	--	--	
1.25	55.7 ± 0.1	Discontinuous		--	--	500.0	255.6 ± 0.5	--	--	
1.5	69.0 ± 2.0	Discontinuous		--	--	500.0	286.3 ± 1.0	--	--	
2	80.2 ± 0.6	Continuous		--	--	500.0	280.9 ± 3.2	16.8 ± 0.3	22.7 ± 0.7	
2.5	92.3 ± 0.5	Continuous		--	--	500.0	299.3 ± 0.4	22.6 ± 2.2	17.0 ± 0.5	

Schematic Representation column (from top to bottom):
- ST1: L_P, h_P, Thread, h_T, d_T, Substrate; $h_P = 250$ nm
- ST2: Thread, h_T, L_T, Substrate
- ST3: Thread, $\theta_{E\text{-}PMMA\text{-}S}$, h_T, Substrate
- ST4: Thread, θ^*, h_T, Substrate, Bread-Loaf Morphology
- ST5: Continuous Film, h_L, a_S, h_F, Substrate

*Cannot be directly measured as no continuous film forms at these conditions on flat substrate due to spin dewetting on a non-wettable substrate
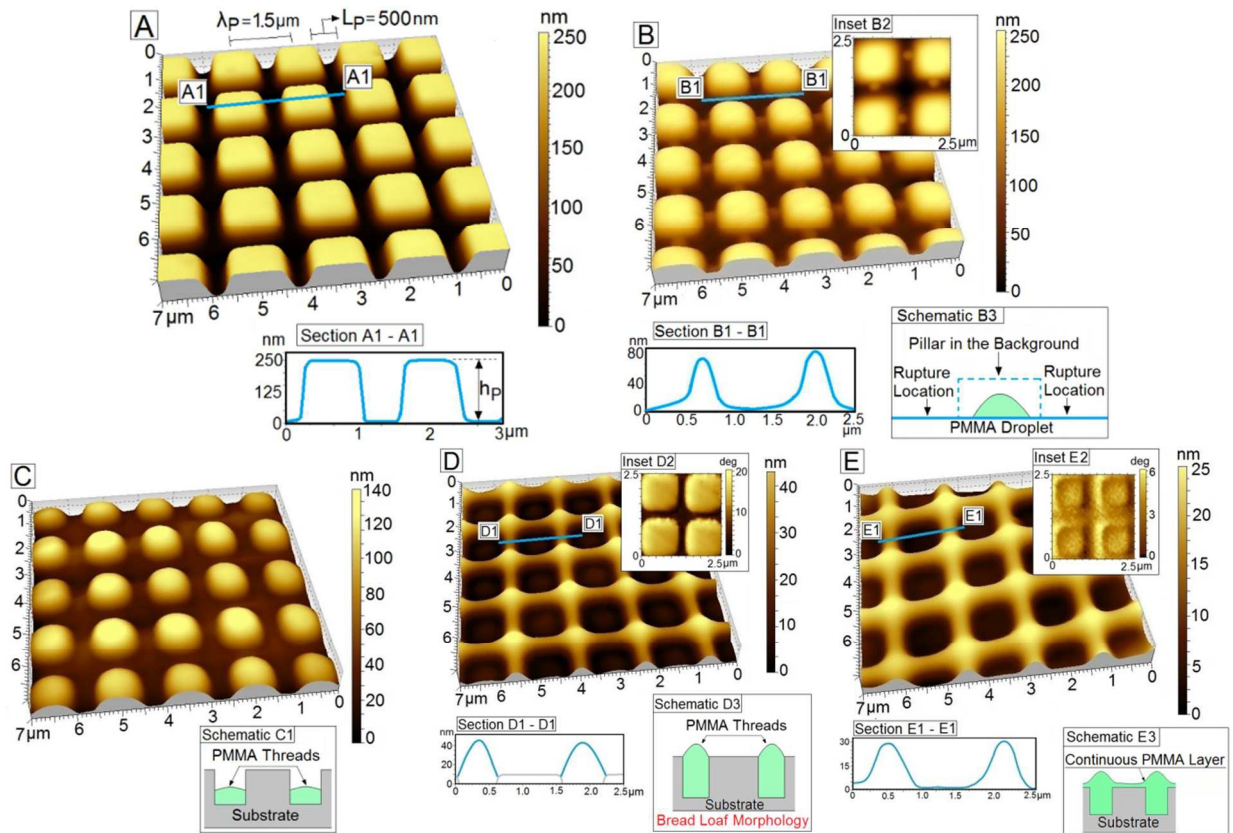
*Fig. 1: (A) AFM image of the patterned substrates used in the experiments. The line width (L_P), periodicity (λ_P) and height of the features are marked in the figure. Inset A1 shows the line profile of the substrate. (B) **Type 1** bottom layer comprising an array of ordered PMMA droplets resulting from spin dewetting of solution with C_{n-PMMA} =0.1%. Inset B2 shows higher resolution image of the droplets. Inset B3 schematically shows the rupture locations during spin dewetting. (C, D) **Type 2** bottom layer (interconnected network of PMMA threads along substrate grooves) for C_{n-PMMA} =0.75% and C_{n-PMMA} =1.5% respectively. Inset D2 shows the phase contrast image showing bare pillar tops. (E) **Type 3** bottom layer (continuous PMMA film with undulating top surface) at C_{n-PMMA} = 2.0%. Inset E2 shows the phase image with no contrast on the pillar tops for a continuous film.*

Results and Discussion

Morphology of the Bottom PMMA Layer

In order to understand the initial morphology and evolution of the bilayer, it is essential to understand the as cast morphology of the bottom layer on the patterned substrate. Fig. 1B – 1E shows how the morphology of the bottom PMMA layer changes as C_{n-PMMA} increases from 0.1% to 2.0%. At very low concentration (C_{n-PMMA} < 0.15%), **Type 1** bottom layer comprising of a well ordered array of equal sized droplets is observed (Fig. 1B). The droplets are located beside

every pillar and have a periodicity λ_D = 1.5µm, which is identical to λ_P, implying that λ_D is entirely controlled by λ_P.[78] Upon increasing $C_{n\text{-}PMMA}$, the morphology of the bottom layer transforms to continuous, inter connected network of threads surrounding each pillar along the substrate grooves. For $0.2\% \leq C_{n\text{-}PMMA} \leq 0.55\%$, the width of the PMMA threads ($L_{T\text{-}PMMA}$) are narrower than that of the width of the grooves (L_P), as shown in Schematic ST2 in Table 1. For $C_{n\text{-}PMMA} > 0.6\%$, PMMA threads span the entire width of the groove ($L_{T\text{-}PMMA} = L_P$) (ST3, Table 1). Additional experiments were performed with $C_{n\text{-}PMMA}$ = 0.55%, 0.60% and 0.70% to identify the critical $C_{n\text{-}PMMA}$ at which this transformation occurs as we will eventually see is that this is extremely important. In the latter regime, $h_{T\text{-}PMMA}$ progressively increases with increase in $C_{n\text{-}PMMA}$. The arch like cross section of the threads is attributed to the partial wetting of the substrate material by the casting solvent.[67] At $C_{n\text{-}PMMA} \approx 1.25\%$, $h_{T\text{-}PMMA}$ becomes comparable to h_P, and for $C_{n\text{-}PMMA} > 1.25\%$, $h_{T\text{-}PMMA}$ exceeds h_P. However, till $C_{n\text{-}PMMA} < 1.75\%$, the PMMA meniscus doesn't spread over the pillar tops (ST4, Table 1) and no continuous film is formed. As a result the intrinsic contact angle between PMMA threads and the pillar edges (Θ^*) exceeds $\Theta_{E\text{-}PMMA\text{-}S}$, as marked in ST4. A continuous PMMA film is observed only when $C_{n\text{-}PMMA} \geq 1.75\%$, resulting in **Type 3** bottom layer. The "bread loaf morphology" (ST4, Table 1) is attributed to strong pinning of the polymer meniscus at the sharp pillar edges. This effect persists even in a continuous, as can be seen in Fig. 1D and 1E.[67] These undulations are located over substrate grooves and are out of phase with respect to the substrate patterns, due to non wettability of the substrate. Interestingly, though both Fig. 1D and 1E qualitatively appear to be rather similar, the corresponding phase images clearly distinguish that the pillar tops are exposed in Fig. 1D, while they are fully covered by PMMA in Fig. 1E.

11

The formation of discontinuous PMMA bottom layers for $C_{n\text{-}PMMA} < 1.75\%$ (Fig. 1B – 1D) is attributed to spin dewetting where the solution layer ruptures and dewets the substrate during spin coating itself.[78] In classical spin coating, deposition of the solute on the substrate starts when the solute attains the saturation concentration (C_{nS}^{*}) in the solution layer during spinning due to progressive evaporation of solvent. Beyond this stage, the solute phase segregates and deposits on the substrate forming a continuous film. However, when the C_n is too low, despite continuous solvent evaporation during spinning, the intrinsic solute concentration (C_n^{*}) never reaches C_{nS}^{*}, and as a consequence the solute never phase segregates. The solvent layer, towards the late stage of spinning becomes very thin and undergoes spontaneous rupture over the substrate, resulting into isolated patches of the solution. On a patterned substrate, the rupture of the solution layer is guided along the contours of the substrate patterns resulting in aligned polymer nano droplets or interconnected network of threads, once the solvent evaporates fully.[78]

Spin Dewetted Type 1D Bilayer

Fig. 2 shows the morphology of the bilayers when solutions with different $C_{n\text{-}PS}$ are coated on Type 1 bottom layers. For $C_{n\text{-}PS} < 0.15\%$, the dispensed PS solution also spin dewets over the substrate pillars and as $S_{PS\text{-}PMMA} > 0$, it gets deposited over the existing PMMA droplets resulting in an array of core-shell droplets (Fig. 2A). Similar ordered array of core-shell droplets by thermal dewetting of a polymer bilayer requires prolonged annealing.[77] In contrast it is realized within few minutes by spin dewetting. This highlights the strength of spin dewetting as an ultra-fast meso fabrication technique, the advantages of which is yet to be harvested fully.

12
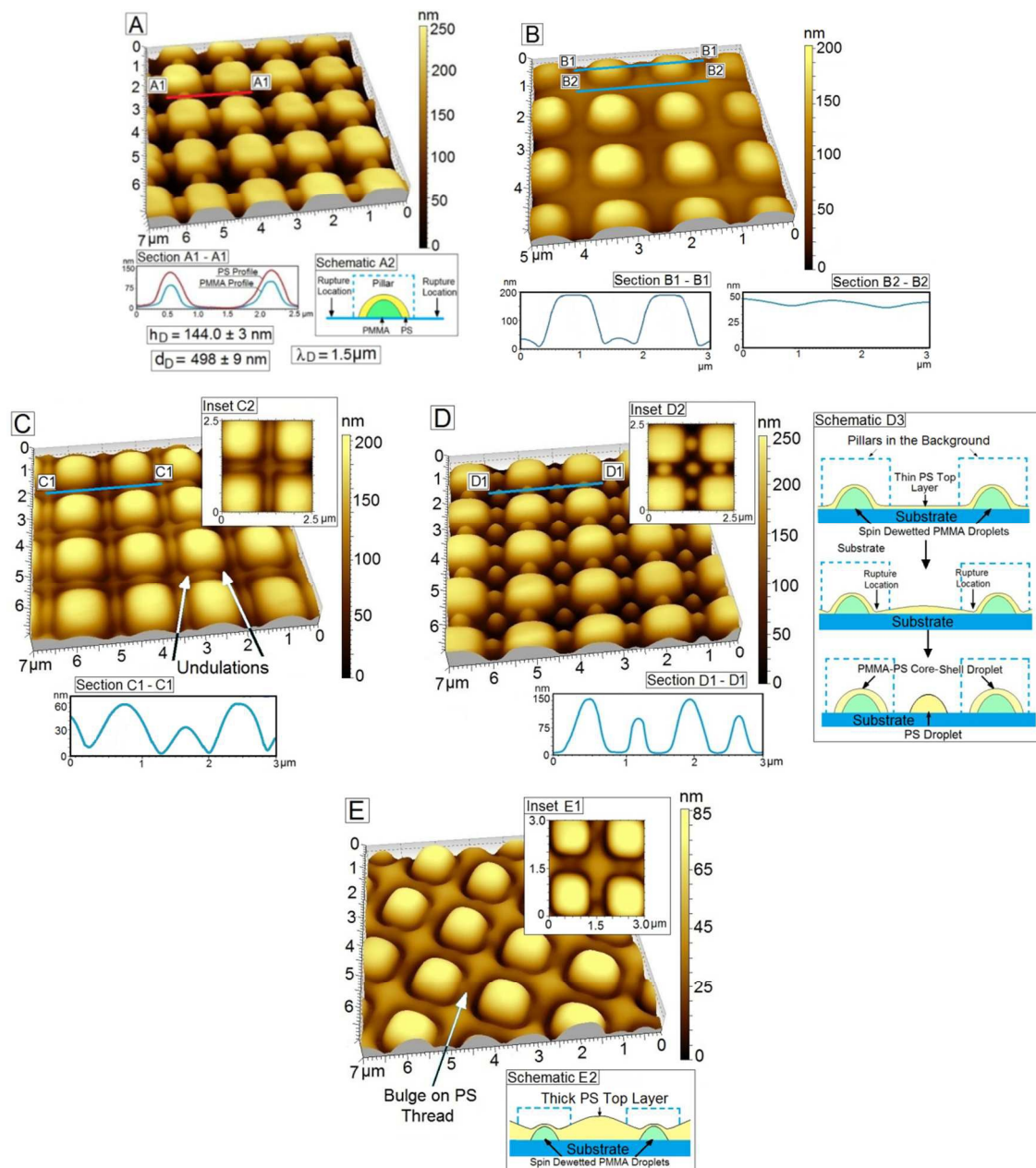
Fig. 2: (A) Aligned array of Core (PMMA)-Shell (PS) droplets resulting from spin dewetting of both the PMMA and PS layers at low solution concentration of $C_{n\text{-}PMMA} = C_{n\text{-}PS} = 0.1\%$. (B) As cast morphology of a Type 2D bilayer with $C_{n\text{-}PS} = 0.25\%$ over a PMMA droplet array obtained by spin dewetting for $C_{n\text{-}PMMA} = 0.1\%$. (C,D) Morphologies of the bilayer (shown in figure 2B) after 45 minutes and 75 minutes of annealing respectively. The morphology shown in frme D comprises of an alternating array of core-shell and PS droplets. Inset D3 shows the schematic representing the process of dewetting. (E) Interconnected network of PS threads over underlying PMMA droplets for $C_{n\text{-}PS} = 1.25\%$, annealed for 12h. Inset E1 shows a magnified image and E2 gives a schematic representation of the morphology. The Type 1 PMMA bottom layer corresponds to $C_{n\text{-}PMMA} = 0.1\%$ in all the frames.

13

With increase in $C_{n\text{-}PS}$, the morphology of the as cast top layer changes to interconnected network of PS threads covering the substrate grooves and the spin dewetted PMMA droplets, which is clearly seen in Fig. 2B. The as cast PS threads observed in figure 2B (for $C_{n\text{-}PS} = 0.25\%$) is devoid of any undulations. Similar to what is observed in PMMA threads previously, for $0.2\% \leq C_{n\text{-}PS} \leq 0.5\%$, $L_{T\text{-}PS} < L_P$ and hence the threads starts to undulate due to Rayleigh Instability upon thermal annealing. Fig. 2C shows the morphology of such PS threads after thermal annealing for 45 minutes. The thread is seen to undulate on both sides of each pre-existing PMMA droplet, where its width is narrowest. Localization of PS over the PMMA droplets occurs at the expense of immediate neighbourhood becoming PS deficient. The threads eventually rupture due to transverse growth of these undulations after 75 minutes of annealing. The ruptured PS thread subsequently retracts along the non wettable substrate grooves, eventually forming droplets due to surface energy minimization (Fig. 2D). The droplet array has $\lambda_D = 750$ nm, which is half of λ_P and clearly highlights miniaturization of λ_D in a bilayer. The array shown in Fig. 2D is also unique as it comprises of alternate droplets of a single polymer (PS at the corners of the grooves) and core–shell drops (beside the pillars). This can be verified from difference in the sizes of the respective droplets from the line scan shown in inset D1 of Fig. 2D. To the best of our knowledge, such ordering has never been achieved before. The likely sequence of formation of the alternate drop array is shown in inset D2 of Fig. 2D.

Further increase of $C_{n\text{-}PS}$ in the range 0.5% – 1.50% leads to the PS threads spanning the entire groove width ($L_{T\text{-}PS} = L_P$). Upon thermal annealing, these PS threads remain stable as there is no space for any undulations to grow due to the presence of the confining substrate walls. This results in final dewetted morphology comprising of an embedded array of PMMA droplets under continuous interconnected network of PS threads, as observed in Fig. 2E which shows the final

morphology of a Type 1 bilayer where $C_{n\text{-}PS}$ = 1.25% after 12h of annealing. This morphology is

obtained right after spin coating and remains nearly unaltered during annealing, except that the

cross section of the PS threads become more rounded ($\theta_{PS\text{-}S}$ increases) in comparison to that in as

cast threads (similar to Fig. 4A). This is attributed to the non wettability of the substrate walls

and as a result the PS contact line recedes downwards along the pillar walls, transferring more

PS towards the centre of the grooves. The presence of the embedded PMMA droplets creates tiny

bulges in the PS threads which are marked in Fig. 2E. For $C_{n\text{-}PS} \geq 1.75\%$, a continuous PS film

forms, which ruptures over the pillar tops during annealing. The PS meniscus retracts over the

substrate grooves resulting in a morphology that is similar to the one shown in Fig. 1D.

Dewetting of Type 2D Bilayers

When PS is spin coated on a Type 2 bottom layer, the generic as cast morphology is always

thread on thread till $C_{n\text{-}PS}$ becomes high enough to form a continuous film (discussed in the next

section). The final dewetted morphology however may vary significantly depending on $h_{E\text{-}PS}$ and

$h_{E\text{-}PMMA}$. Fig. 3A shows a unique morphology obtained in dewetting of a stacked layer of very

thin network of interconnected threads having $C_{n\text{-}PMMA} = C_{n\text{-}PS} = 0.25\%$. The PMMA threads first

ruptures under an intact PS layer at the corners of the pillars. The rupture occurs at the corners as

the threads are least pinned at these locations, as compared to any other location between the two

adjacent pillars. The ruptured PMMA threads retract inwards along the grooves. This allows the

intact PS thread to come in direct contact with the substrate at the locations where the PMMA

layer has ruptured. As $S_{PS\text{-}Sub} < 0$, the thin PS threads also rupture over the same locations

resulting in a true hole and the PS meniscus also retracts inwards.
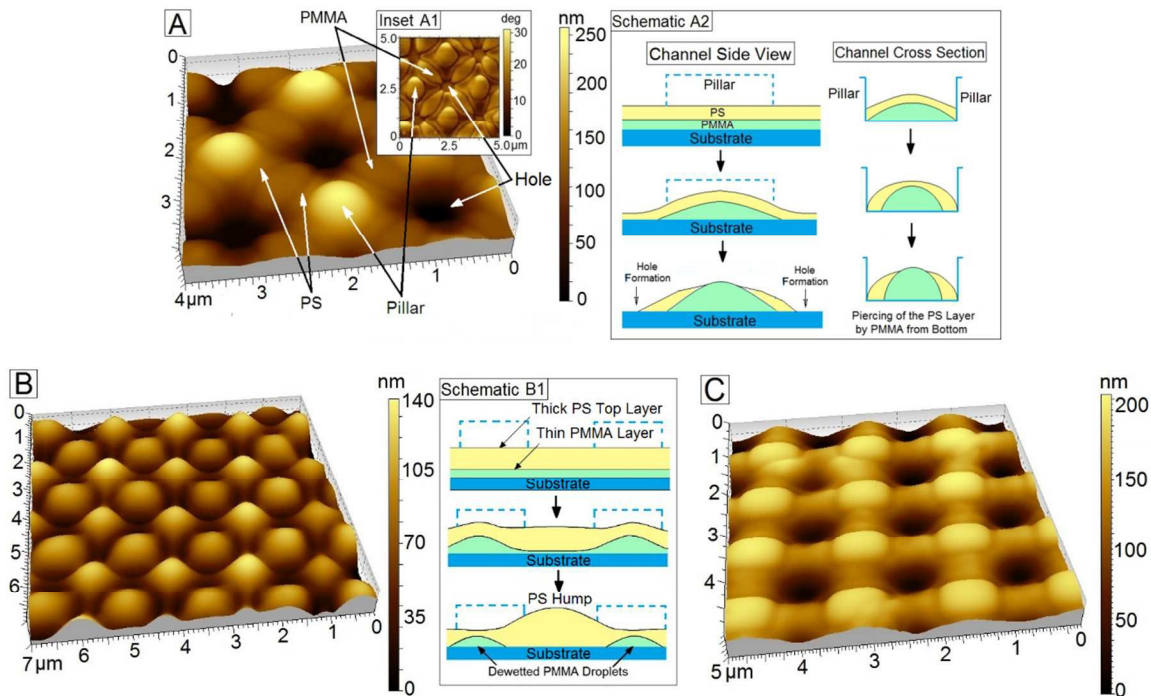
Fig. 3: *Morphology of dewetted **Type 2D** thread on thread bilayers (A) Cast from $C_{n\text{-}PMMA} = C_{n\text{-}PS} = 0.25\%$, and annealed for 15h. Inset A1 shows the corresponding phase image and inset A2 shows the evolution process schematically from twp orthogonal angles. (B) Cast from $C_{n\text{-}PMMA} = C_{n\text{-}PS} = 0.5\%$ after 17h of annealing. Inset B1 shows the schematic of the process. (C) Morphology of underlying PMMA layer after selective removal of PS top layer.*

The inward retraction of PMMA threads results in increase of the local height of the PMMA domain within the grooves. The height increase of the PMMA domains exerts a pressure on the intact portion of PS threads, eventually piercing it from the bottom (shown in the last frame of inset A2). The confined nano scale dynamics of the two sequentially ruptured polymer threads results in a unique morphology comprising of holes at the pillar corners, and both the polymers accumulate within the grooves between adjacent pillars. Piercing of the PS thread by the rising PMMA meniscus results in laterally co-existing domains of PMMA and PS. The elongated PMMA domain in the middle of the groove is isolated from the pillars by thin strips of PS on both sides. The complexity of the morphology can be clearly understood from the phase contrast image shown in inset A1 of Fig. 3A. The evolution sequence is schematically shown in inset A2 of Fig. 3A. The final morphology is obtained after 15h of annealing. The extremely slow

16

dynamics is attributed to flow of PMMA and PS in opposite directions during piercing of the PS top layer, which is associated with high interfacial shear stress between two high viscosity polymers.

The interconnected network of PMMA threads continues to rupture at the pillar corners till $C_{n\text{-}PMMA} \leq 0.55\%$ ($h_{E\text{--}PMMA} = 22.7$ nm, $h_{T\text{--}PMMA} = 71.3$ nm), and thus the initial dynamics of any bilayer with $C_{n\text{-}PMMA} \leq 0.55\%$ remains nearly identical to that discussed in the context of previous figure. For $C_{n\text{-}PMMA} \geq 0.60\%$, the PMMA threads becomes adequately thick ($h_{T\text{--}PMMA} \geq 109.3$ nm), spans the entire substrate groove ($L_{T\text{--}PMMA} = L_P$) and as a consequence the rupture in the PMMA network gets supressed. Even for $C_{n\text{-}PMMA} \leq 0.55\%$, the evolution sequence of the top layer changes drastically as $C_{n\text{-}PS}$ exceeds 0.50%. A thicker PS layer does not immediately rupture after coming in contact with the substrate at the corners, where the PMMA thread network has previously ruptured. On the other hand, the inward retraction of the PMMA meniscus (Schematic B1, Fig. 3B) exerts a pressure on the PS threads from the bottom. Though the thicker PS domains do not rupture any more, the pressure from the bottom engenders an outward flow of PS leading to its accumulation at the corners, resulting in PS humps over there. The morphology remains unaltered even after 24h of annealing. The rupture of the PMMA threads at the corners is verified from Fig. 3C which shows the morphology of the sample after selective removal of PS. Such morphology can be ideal as a template for the fabrication of ordered non closed pack array of colloidal particles, as the colloids are expected to preferentially immobilize over the holes. The generic morphology observed in Fig. 3 persists for a wide range of $C_{n\text{-}PS}$ as long as $C_{n\text{-}PMMA} \leq 0.55\%$. As a result of pinning and high interfacial shear stress at the PS – PMMA interface, the submerged PMMA domains in Fig. 3 are often not hemispherical and tend to become elongated along the direction of the groove.

It is already mentioned that for higher $C_{n\text{-}PMMA}$, the rupture of the PMMA threads at the corners gets suppressed. A thread might rupture following two mechanisms, either due to amplification surface capillary waves as is observed in case of Fig. 3A, or due to Rayleigh instability as observed in Fig. 2B. The strength of the dispersive interfacial interaction becomes weak as $C_{n\text{-}PMMA}$ (vis-a-vis $h_{T\text{-}PMMA}$) increases and thus the growth of surface fluctuations becomes weak, failing to cause rupture. On the other hand, the transverse undulations fail to grow if the threads span the entire width of the groove, eventually suppressing Rayleigh instability.[68] As both the mechanisms become ineffective, threads with higher $C_{n\text{-}PMMA}$ become completely stable within the grooves. Since PS wets PMMA, the PS threads atop the PMMA threads remain in conformal contact without exhibiting any evolution.
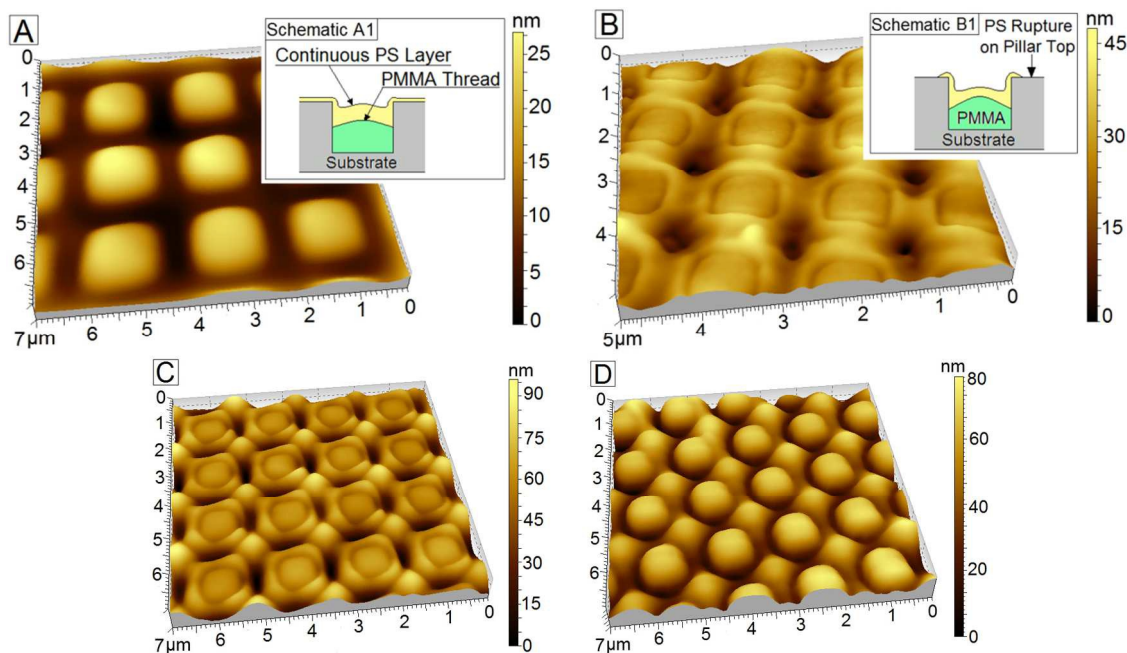
Fig. 4: *(A) As cast morphology of a Type 2C Bilayer obtained from $C_{n\text{-}PMMA}$ = 0.5% and $C_{n\text{-}PS}$ = 1.5%. Inset A1 schematically shows the cross sectional morphology of the bilayer. (B–D): Progressive evolution of the bilayer after 30 minutes, 4 hours and 17 hours of thermal annealing, respectively. Inset B1 schematically shows the conformation of the PS meniscus after rupture.*

Dewetting of Type 2C Bilayers

As $C_{n\text{-}PS}$ increases the top PS layer becomes continuous covering the submerged interconnected network of PMMA threads and the morphology of the as cast bilayer changes from Type 2D to

Type 2C. Due to the presence of the pre-existing PMMA threads, the PS solution is dispensed on an effective substrate with periodic variation in both topography and wettability. The initial morphology of a Type 2C bilayer can be broadly sub-divided into two categories depending on whether $h_{T\text{-}PMMA}$ is much lower than h_P or $h_{T\text{-}PMMA}$ is comparable to h_P, as subsequent discussion shows that the dewetted morphology differs significantly under these two settings. Fig. 4 shows the gradual evolution of a Type 2C bilayer of the first type obtained by coating a solution with $C_{n\text{-}PS} = 1.5\%$ ($h_{E\text{-}PS} = 69.0$ nm) over a bottom layer that corresponds to $h_{E\text{-}PMMA} = 21.1$ nm ($h_{T\text{-}PMMA} = 68.9$ nm). The as-cast morphology of the bilayer is shown in Fig. 4A. The qualitative cross sectional morphology of the bilayer is schematically shown in inset A1 of Fig. 4A. Upon thermal annealing, the PS layer ruptures over the non wettable pillar tops, with subsequent outward retraction of the PS contact line towards the pillar edges, which is seen in Fig. 4B after 30 minutes of thermal annealing. After 4 hours of annealing, humps of PS appear at the corner of the pillars (Fig. 4C). The formation of hump is attributed to the rupture of the PMMA thread network at the pillar corners following the mechanism discussed earlier in the context of Fig. 3B. Fig. 4D shows the final morphology after 17h of annealing, where the pillar tops are completely devoid of PS and are surrounded by polymer threads along the substrate grooves with prominent humps at the corners (similar to Fig. 3B).

Fig. 5 shows the dewetting of Type 2C bilayer of the second type, i.e. when $h_{T\text{-}PMMA} \approx h_P$. This is obtained when the PMMA bottom layer is cast from a solution with $C_{n-PMMA} = 1.25 \%$ ($h_{E-PMMA} = 53.2$ nm), which results in $h_{T-PMMA} \approx 262.1$ nm. As the grooves are filled with an interconnected network of PMMA threads, the topographic contrast on the effective substrate while coating the PS top layer is now much less, and a continuous PS film forms at much lower $C_{n\text{-}PS}$ as compared to that required for obtaining a continuous top layer in the previous case. The

morphology of the bilayer after casting the top PS layer from a solution with $C_{n\text{-}PS} = 0.5\%$ ($h_{E\text{-}PS}$ = 22.3 ± 0.4 nm) is shown in Fig. 5A. The continuous PS film has an undulating top surface with the undulations being in phase with the morphology of the submerged interconnected network of PMMA threads. Upon thermal annealing the PS film ruptures over each substrate pillar and the PS contact line retracts, accumulating over the PMMA threads, which is shown in Fig. 5B. As $L_{T\text{-}PMMA} = L_P$, the morphology of the PS – PMMA bilayer threads remains unaltered beyond this stage despite prolonged annealing.
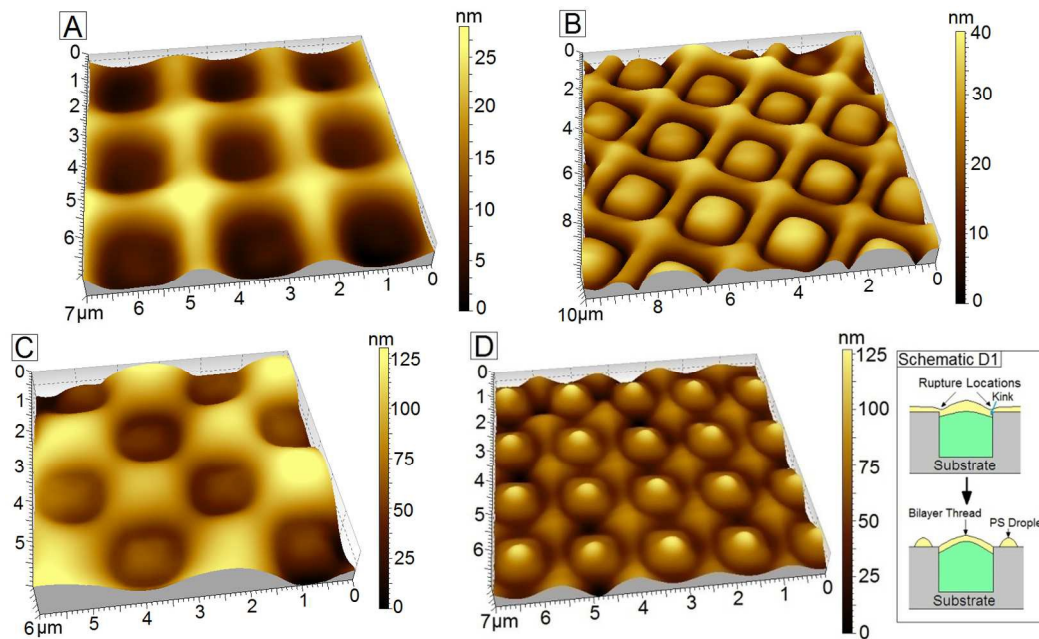
Fig. 5: (A) As cast morphology of a Type 2C bilayer obtained by sequentially coating solutions with $C_{n\text{-}PMMA}$ = 1.25% and $C_{n\text{-}PS}$ = 0.5%. (B) Morphology after dewetting for 2.5h comprising an interconnected network of bilayer threads. (C) Dewetted morphology after 3h of a bilayer obtained by coating $C_{n\text{-}PS}$ = 1.0 %.($h_{E\text{-}PS}$ = 41.8 nm) on a bottom layer that is identical to Fig. 5A. (D) Dewetted morphology (6h annealing) of a Type 2C bilayer cast from $C_{n\text{-}PMMA}$ = 1.0% and $C_{n\text{-}PS}$ = 1.0 %.

Fig. 5C shows how the dewetted morphology changes with gradual increase in $h_{E\text{-}PS}$ on the same PMMA bottom layer as in Fig. 5A. Fig. 5C shows that for a thicker PS film ($h_{E\text{-}PS}$ = 41.8 ± 0.7 nm), the film ruptures over every second pillar forming a checkerboard pattern. For a film with $h_{E\text{-}PS}$ = 41.8 nm, λ_D is of the order of 4.5 μm on a flat substrate, which is higher than λ_P.[65] As a result, the film is seen to rupture over every second pillar, implying that the effective wavelength

of the ruptured holes on the patterned substrate is a resultant of competition between $\lambda_{D\text{-}FILM}$ and λ_P. The formation of the checkerboard structures is also associated with localisation of dislodged PS over the neighbouring pillar tops, where the local PS layer thickness goes up significantly, and thus the film never ruptures at these locations. This regime continues till $h_{E\text{--}PS} \approx 69$ nm. For even thicker PS top layers ($h_{E\text{--}PS} \approx 81$ nm), the film is seen to rupture over fewer number of pillars randomly (image not shown) before becoming completely stable for $h_{E\text{-}PS}$ in the range of 100 nm or more. The stability was tested with at least 7 samples having PS film thickness in the range of 100 to 130 nm by annealing for more than 48 hours on substrates comprising PMMA threads as bottom layer. This is a completely unexpected observation, as pattern directed dewetting is always associated with ordering of dewetted structures and not film stabilization. This observation in fact opens up the possibility of using a physico-chemical patterned substrate for stabilizing a thin film. We argue that the presence of the elevated PMMA rims around the pillar tops, over which the PS film is stable, imparts overall stability to the thicker PS films. This is discussed in details in the context of Fig. 6.

A special situation arises in a Type 2C bilayer when the $h_{T\text{-}PMMA}$ is slightly lower than h_P (shown schematically as an inset Fig. 5D), obtained by coating a solution with $C_{n\text{--}PMMA} = 1.0\%$. This results in small kinks close to the pillar edges in the continuous PS film as the height of submerged interconnected network of PMMA threads is just lower than h_P. When dewetting is engendered in the PS film ($h_{E\text{-}PS} = 41.8$ nm), it is seen that the PS film ruptures along the edges of the pillars. This is in clear contrast to that observed in Fig. 5A where the film ruptures on the top of the non wettable pillars. The presence of the kink around the pillar edges coupled with differential wettability between substrate and PMMA threads triggers localized rupture of the PS film along the contour of the kink. As a result, part of the PS film gets isolated on the pillar tops,

which eventually retract inwards forming PS droplets over each pillar. The other part of the detached PS film remains localized over the PMMA thread network. The final morphology comprises of PS droplets on pillar tops surrounded by interconnected network of bilayer threads over the grooves. The diameter of the PS droplets gradually increases with increase in $h_{E–PS}$ for the same PMMA bottom layer.

Interestingly, the annealing durations mentioned in frames B, C and D of figure 5 are different, which correspond to the annealing time at which the final morphology is observed. Beyond this stage, the morphology remains unaltered even upon further annealing. The longer time required in figure 5C is attributed to a thicker PS film. The dewetting of the ruptured PS segments on top of the Pillars is responsible for much slower dynamics in case of figure 5D.

Dewetting in Type 3C bilayer

Fig. 6A shows the typical morphology of a Type 3C bilayer where both the layers are continuous. The PMMA bottom layer becomes continuous for $C_{n–PMMA} \geq 2.0\%$ ($h_{E\text{-}PMMA} \geq 74.0$ nm). The film has an undulating top surface as schematically shown in ST5 of Table 1. PS films of all thickness are continuous on a continuous PMMA bottom layer. With increase in h_E of either layer, the undulation amplitude (a_S) progressively reduces and the film tends to become flatter. When annealed, the thinnest part of the PMMA film above the pillars ruptures first resulting in an outward retraction of the PMMA contact line towards the pillar edges under an intact PS layer, which now comes in direct contact with the substrate at the pillar tops. The retraction of the PMMA meniscus is slow due to high frictional resistance at the PS – PMMA interface. After 3h of annealing, the PS film also ruptures over the substrate pillars and retracts outwards resulting in bilayer threads over the substrate grooves. Fig. 6B shows the final dewetted morphology of a bilayer comprising of $h_{E\text{-}PMMA} = 74.0$ nm and $C_{n\text{-}PS} = 0.25\%$ after 8 hours of

annealing. The image clearly shows that the pillar tops are devoid of any polymer and are surrounded by an interconnected network of bilayer threads. With increase in $h_{E\text{-}PMMA}$, the extent of retraction of the PMMA contact line reduces and it gets pinned close to the edge of the pillar periphery, as can be seen in the inset B1 of Fig. 6B for a film with $h_{E\text{-}PMMA} \sim 100$nm. The outward retraction of the contact line gets hindered as further accumulation of PMMA over the grooves lead to higher curvature and hence higher Laplace pressure, which opposes the outward retraction. Similarly, the PS contact line may or may not fully retract depending on $h_{E\text{-}PS}$. The fraction of the pillar top exposed after dewetting reduces with enhancement of either $h_{E\text{-}PMMA}$ or $h_{E\text{-}PS}$.
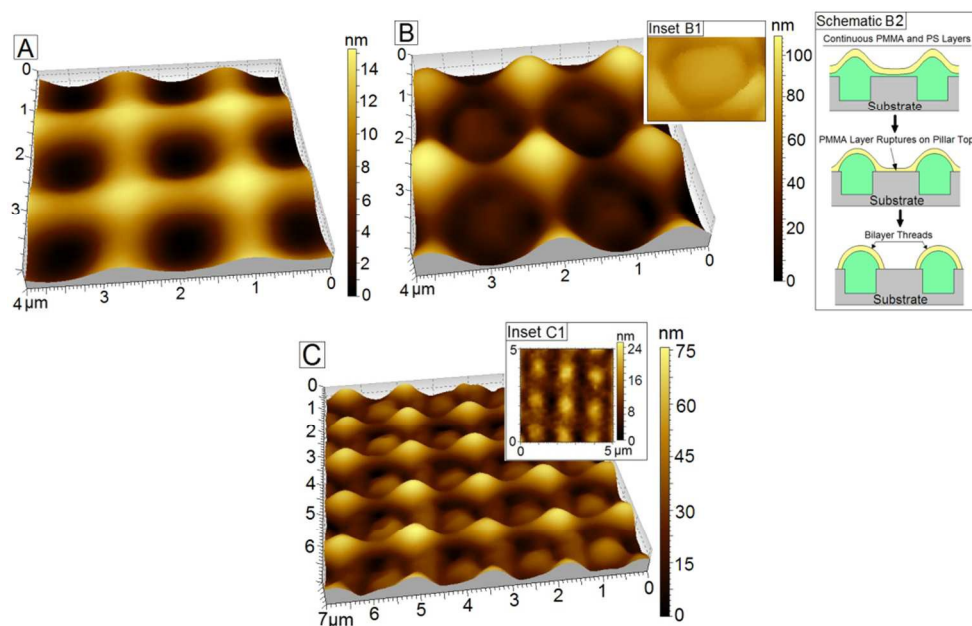
Fig. 6: *(A) As cast morphology of a **Type 3** bilayer obtained by sequential spinning of solutions with $C_{n\text{-}PMMA}$=2.0 % and $C_{n\text{-}PS}$=0.25 %. (B) Dewetted morphology after 8h of thermal annealing showing the exposed pillar tops. Inset B2 schematically shows the intermediate dewetting stages. Inset B1 shows that the PS contact line does not retract fully and remains pinned over the pillars for higher $C_{n\text{-}PS}$= 1.0 %. (C) Morphology of the extracted dewetted PMMA bottom layer after selectively removing the intact PS film in a Type 3 bilayer with $C_{n\text{-}PMMA}$=2.0 % and $C_{n\text{-}PS}$=1.5 %. Inset C1 shows the morphology with the intact top PS film. The film shown in this frame was annealed for 24 hours.*

In order to understand the effect of top layer thickness on the evolution of the bilayer, $h_{E\text{-}PS}$ is progressively increased keeping $h_{E\text{-}PMMA}$ fixed at 74.0 nm. The PS film ruptures over each pillar

top till $h_{E\text{-}PS}$ = 55.7 nm ($C_{n\text{-}PS}$ = 1.25 %). For $h_{E\text{-}PS}$ ≥ 69.0 nm ($C_{n\text{-}PS}$ = 1.5 %) the PS layer becomes completely stable, which can be seen in the inset C1 of figure 6C. Fig. 6C shows that the PMMA layer has ruptured and dewetted under an intact PS film, which is revealed upon selective removal of the top PS layer. The transition from an unstable to a stable PS top layer occurs at a critical $C_{n\text{-}PS}$ which gradually decreases with increase in $C_{n\text{-}PMMA}$. Unlike Fig. 5, no checkerboard pattern is observed in this case. The presence of the curved wettable PMMA domains prevents the retraction of PS, even if the film ruptures over a non wettable pillar top. It is worth pointing out that in the context of Fig. 5C, $h_{T\text{-}PMMA}$ ≈ h_P and therefore the PMMA threads cannot physically impose a barrier to the retracting PS meniscus and subsequent redistribution of PS, resulting in the checkerboard pattern. However, as the initial bottom layer is continuous in the present case, the PMMA threads formed after rupture and dewetting of the bottom layer are significantly higher (compared to bread loaf morphology). This in turn prevents redistribution of PS over other pillars. If the PS top layer is thicker, due to a competition between $\lambda_{D\text{-}FILM}$ and λ_P, the film ruptures over some random locations instead of each pillar top. Also in order for a hole to appear at the location of rupture, the dislodged PS needs to be physically redistributed to other intact areas (over other pillar tops). This action is strongly affected by the presence of the elevated PMMA threads around each pillar, screening the flow of the PS which adds stability to the thicker PS films. In thinner films, as λ_D is not much higher λ_P and rupture takes place over every pillar, without requiring PS to cross the PMMA barriers.

Discussion

In order to understand the influence of the thickness as well as the as cast morphology on the ordering process, we identify the distinct final morphologies observed in the experiments and list them in Table 2.

24

Table 2: List of final dewetted morphologies observed

Sl. No.	Description of the Final Morphology	Symbol used in Fig. 7
Common Morphologies		
C1	Intact PS thread over submerged PMMA domains (spin dewetted/ dewetted)	△
C2	Intact PS thread over intact submerged PMMA threads	☐
Rare/Unique Morphologies		
U1	Core-shell droplet array	○
U2	Alternate droplet array (single polymer – core shell)	●
U3	Laterally coexisting PS & PMMA domains with hole at the corners	▽
U4	PS thread on intact submerged PMMA thread along with PS droplet on each pillar top	⊡
U5	Checkerboard pattern in continuous PS layer	◧
U6	Random rupture of PS film over some pillars	◨
U7	Stable PS film	⃞s
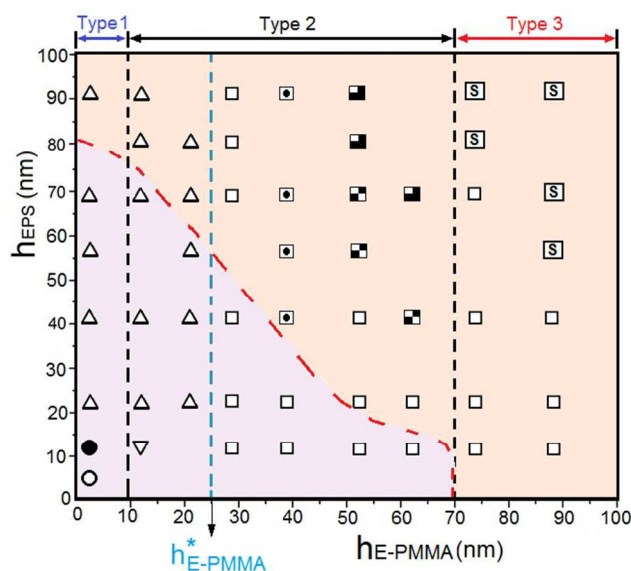
Fig. 7: *Morphology phase diagram as a function of the individual layer thickness. The demarcating lines act as guides only. The red dotted line represents a transition between discontinues to continuous PS top layer, and is based on experimental observation only. The symbols are mentioned in Table 2.*

We also construct a morphology phase diagram in Fig. 7, where the distinct morphologies identified with different symbols are mapped in a plot that has h_{E-PMMA} and h_{E-PS} as the two coordinate axes. In the phase diagram certain generic morphologies persist over a wide range of

25

combinations of h_{E-PMMA} and h_{E-PS} which are termed as "common morphologies" in Table 2 and are identified with prefix **C.** In contrast, few morphologies are observed only for a narrow range of h_{E-PMMA} and h_{E-PS}, which are termed as "uncommon morphologies" (prefixed with **U**). It can be clearly seen in Fig. 7 that the phase diagram is dominated by two specific dewetted morphologies, *C1* and *C2*. However, there is a clear transition between regions that are dominated by these two morphologies which is distinguished by a vertical line (shown with the blue dotted line) that corresponds to $h^*_{E-PMMA} \approx 25.1$ nm. This critical thickness demarcates between spin dewetted PMMA threads that are narrower than the substrate width ($L_{T-PMMA} < L_P$ for $h_{E-PMMA} < h^*_{E-PMMA}$) and the threads that span the entire width of the grooves ($L_{T-PMMA} = L_P$ for $h_{E-PMMA} > h^*_{E-PMMA}$). In case $h_{E-PMMA} > h^*_{E-PMMA}$, there is no dynamics within the grooves and dewetting primarily takes place over the pillars. Within this regime, with gradual increase of h_{E-PS} the condition changes from no evolution during annealing (both layers formed by spin dewetting) to rupture and dewetting of only PS top layer (for Type 2C films) or that of both the layers (for Type 3C films). For $h_{E-PMMA} < h^*_{E-PMMA}$, the threads evolve within the grooves with associated rupture of the PMMA threads and its retraction except for very low h_{E-PMMA}, where the bottom layer has already spin dewetted to droplets. In case the PMMA threads or domains rupture below an intact PS film or thread, the dynamics of the system is observed to be extremely slow due to high interfacial frictional resistance at the polymer – polymer interface. Thus, it becomes clear that while the generic morphology is influenced much by the effective thickness of the PMMA bottom layer, particularly whether h_{E-PMMA} is lower or higher than h^*_{E-PMMA}, the dynamics of the system is strongly influenced by the initial morphology of the bilayers.

The unique or rare morphologies also highlight several important and novel issues associated with dewetting of a bilayer on a cross patterned substrate. For example, morphology *U7*

highlights an unexpected yet rather important aspect in the form of generating stable top layers. This is a completely new observation as dewetting of a single layer on a patterned substrate is invariably linked with forced rupture of the film along the contours of the template and ordering of the structures. However, the presence of two layers during evolution generates intrinsic templates which have periodic variation in topography as well as wettability. It turns out that the rupture gets suppressed when there is a confining boundary of a non wettable region by a wettable layer with higher elevation. The surrounding wettable domains act as physical boundary layers and prevent growth of nucleated holes over the non wettable regimes, imparting stability to the top layer. This aspect surely needs further investigation and might lead to a new approach for stabilizing thin polymer films, which is extremely important from the stand point of ultra-thin coatings. The checkerboard patterns (*U5*) are also an example where a competition between different lengths scales ($\lambda_{D\text{-}FILM}$ and λ_P) manifest in suppression of instability over certain nearest neighbour pillars, resulting in a very unique and ordered morphology. This shows the additional tuning ability of the dewetted morphology by simply varying the thickness of different layers in topography mediated bilayer dewetting.

The morphology *U4* is in fact rather similar to *C2* with the additional presence of the PS droplets on the pillar tops. This shows the importance of precise initial morphology of the as cast bilayer in guiding the instability pathways and eventually the final dewetted patterns. As discussed in the context of Fig. 5D, the presence of the tiny kink surrounding each pillar forces the PS film to rupture along the contours of the pillar edge, rather than at the middle of the non wettable pillars as has been observed in most other cases shown in Fig. 5 and Fig. 6. Similarly, the complicated morphology *U3* comprising laterally coexisting domains of PMMA threads surrounded by PS stripes is in many ways a special case of morphology *C1*, where the thin PS threads is pierced

due to upward movement of the submerged PMMA domains. The droplet array (morphology *U2*) comprising of PS drop and PS-PMMA core shell drops arranged in an alternating order is yet another example of how initial conditions can guide the evolution sequence leading to something extraordinarily novel. Such an array comprising of a single and a core – shell nano droplet having precise alternating order has never been realized before. The other important aspect of this specific morphology worth highlighting is the miniaturization achieved in terms of pattern periodicity. It is well known that by dewetting a film on a patterned substrate, it is possible to create structures that replicate the periodicity of the substrate patterns under appropriate conditions. However, we observe in Fig. 2D that the periodicity of the droplets $\lambda_D = 750$ nm which is half of $\lambda_{D\text{-}FILM}$. Such additional miniaturization is not possible in dewetting or in spin dewetting of a single layer on a topographically patterned substrate, and emphasizes the effect of bilayer dewetting on a topographically patterned substrate as a technique for creating novel meso-scale morphologies.

The only work reported on bilayer on topographically patterned surface based on 3-D simulations predicts that for a low surface energy substrate with specific periodicity, an ordered array of droplets encapsulated by the upper layer is formed in the valleys at the late stages of dewetting.[71] Our experimental results complement these observations (like Type 1D and 2D bilayers), but also reveal the existence of far more complicated dynamics and rich structures under different conditions.

Conclusion

In this article, we investigated dewetting of a thin polymer bilayer on a topographically patterned substrate comprising array of square pillars, which has never been explored before experimentally. The most significant parameter that influences the final morphology of the

dewetted patterns is whether the interconnected network of bottom PMMA threads fills the

substrate groove completely or not. In addition to ordering of the instability patterns which is

quite well known in the context of dewetting of a single layer film on a topographically patterned

substrate, this work highlights several important findings which are attributed only to the

presence of a deformable confined interface between the two layers. The patterns reflect the rich

dynamics associated with the nano scale flow of two stacked polymer layers under extreme

lateral confinement. Previous work on dewetting of a single film on a cross patterned substrate

revealed perfect ordering is possible only for a very narrow range of film thickness.[65] In contrast,

we show that ordering persists over a wide range of film thickness combinations leading to a rich

catalogue of structures, and significant miniaturization of feature dimension and feature

periodicity (λ_P) is observed, which have not been realized earlier, based on dewetting.[83] Such

patterns with suitable functional materials might find wide applications in sensors, sustained

drug eluding scaffolds (particularly all the embedded structures), photovoltaic devices etc.

The other important observation is the enhanced stability of the top PS layer over a partially

dewetted PMMA bottom layer, where PMMA threads are localized along substrate grooves.

Under certain conditions, the bottom layer self organizes around each substrate pillar acting like

a physico–chemically patterned template that suppresses the growth of any nucleated hole in the

intact top layer. This result might lead to a new stabilization strategy of ultra-thin films, beyond

the only known approach of stabilizing them with the addition of nano filler particles. Finally, to

show the precise dependence of the dewetted morphology on h_{E-PMMA} and h_{E-PS}, we construct a

morphology phase diagram which highlights the role of h^*_{E-PMMA}. The transitions in the phase

diagram are limited by the discrete experimental data and represent a specific combination of

template geometry and surface energy as the morphology of the dewetted structures would

depend on host of other parameters which include substrate pattern geometry, dimension, duty ratio, wettability etc. However, we do expect the gradual transformation in morphology of the dewetted features with variation of h_{E-PMMA} and h_{E-PS} to broadly follow similar trend even with change in other parameters.

As a final summary, we show that in combination with top down lithography, myriad of novel structures can be obtained by dewetting of a bilayer. Fabrication of so many different structures would ideally require several different templates. More importantly, some of the structures are beyond the scope of realization of any lithography techniques. This is the key strength of the work from the standpoint of fabrication, in addition to unravelling rich physics associated with the dynamics of two stacked ultra thin films under extreme lateral confinement.

Acknowledgement

NOMENCLATURE

d_D	average diameter of dewetted droplets, nm
h_D	height of dewetted droplet, nm
h_E	equivalent thickness of spin-cast flat film, nm
L_P	line width of patterns, nm
L_T	polymer thread diameter, nm
h_P	feature height of patterns, nm
h_T	polymer thread height, nm
h^*_E	critical equivalent film thickness above which polymer threads span the entire substrate grooves, nm
a_S	amplitude of undulations in a continuous film over a topographically patterned substrate, nm

30

T_g	glass-transition temperature of polymer, K
C_n	concentration of polymer solution, (%, wt/volume)
C_{nS}^{*}	saturation concentration, (%, wt/volume)
C_n^{*}	intrinsic concentration of the polymer solution, (%, wt/volume)

Greek Letters

$\lambda_{D\text{-}FILM}$	natural length scale of instability in dewetting of a thin film on a flat substrate, nm
λ_P	periodicity of the pillars, nm
λ_D	periodicity of dewetted droplet array, nm
γ_S	surface energy, mJ/m^2
θ_E	equilibrium contact angle, (°)
θ^{*}	intrinsic contact angle between PMMA threads and the substrate pillar edge, (°)

31

REFERENCES

1. R. Xie, A. Karim, J. F. Douglas, C. C. Han and R. A. Weiss, *Phys. Rev. Lett.*, 1998, **81**, 1251−1254.

2. A. Sharma and R. Khanna, *Phys. Rev. Lett.*, 1998, **81**, 3463−3466.

3. R. Seemann, S. Herminghaus, K. Jacobs, *Phys. Rev. Lett.*, 2001, **86**, 5534−5537.

4. G. Reiter, *Phys. Rev. Lett.*, 1992, **68**, 75−78.

5. K. Jacobs, S. Herminghaus and K. R. Mecke, *Langmuir*, 1998, **14**, 965−969.

6. A. Sharma and G. Reiter, *J. Colloid Interface Sci.,* 1996, **178**, 383–399.

7. A. Ghatak, R. Khanna, and A. Sharma, *J. Colloid Interface Sci.,* 1999, **212**, 483–494.

8. P. Müller-Buschbaum, J. S. Gutmann and M. Stamm*, Phys. Chem. Chem. Phys.*, 1999, **1**, 3857−3863.

9. R. Konnur, K. Kargupta, and A. Sharma, *Phys. Rev. Lett.*, 2000, **84**, 931−934.

10. J. Becker, G. Grün, R. Seemann, H. Mantz, K. Jacobs, K. R. Mecke and R. Blossey, *Nat. Mater.*, 2003, **2**, 59−63.

11. A. Sharma, *Eur. Phys. J. E,* 2003, **12**, 397–408.

12. G. Reiter, M. Hamieh, P. Damman, S. Sclavons, S. Gabriele, T. Vilmin and E. Raphaël, *Nat. Mater.*, 2005, **4**, 754–758.

13. K. A. Barnes, A. Karim, J. F. Douglas, A. I. Nakatani, H. Gruell, E. J. Amis, *Macromolecules*, 2000, **33**, 4177−4185.

14. R. Mukherjee, S. Das, A. Das, S. K. Sharma, A. K. Raychaudhuri, A. Sharma, *ACS Nano*, 2010, **4**, 3709−3724.

15. S. Roy, D. Bandyopadhyay, A. Karim and R. Mukherjee, *Macromolecules*, 2015, **48**, 373−382.

16. C. Maldarelli, R. K. Jain, I. B. Ivanov and E. Ruckenstein, *J. Colloid Interface Sci.*, 1980, **78**, 118–143.

17. F. Brochard-Wyart, P. Martin and C. Redon, *Langmuir*, 1993, **9**, 3682−3690.

18. A. Pototsky, M. Bestehorn, D. Merkt and U. Thiele, *Phys. Rev. E*, 2004, **70**, 025201.

19. D. Bandyopadhyay, R. Gulabani and A. Sharma, *Ind. Eng. Chem. Res.*, 2005, **44**, 1259−1272.

20. D. Bandyopadhyay and A. Sharma, *J. Chem. Phys.*, 2006, **125**, 054711.

21. D. Bandyopadhyay and A. Sharma, *J. Phys. Chem. B*, 2008, **112**, 11564−11572.

22. A. Faldi, R. J. Composto and K. I. Winey, *Langmuir*, 1996, **11**, 4855−4861.

23. P. Lambooy, K. C. Phelan, O. Haugg, and G. Krausch, *Phys. Rev. Lett.*, 1996, **76**, 1110–1113.

24. S. Qu, C. J. Clarke, Y. Liu, M. H. Rafailovich, J. Sokolov, K. C. Phelan and G. Krausch, *Macromolecules*, 1997, **30**, 3640−3645.

25. M. Sferrazza, M. Heppenstall-Butler, R. Cubitt, D. Bucknall, J. Webster, R. A. L. Jones, *Phys. Rev. Lett.*, 1998, **81**, 5173–5176.

26. R. A. Segalman and P. F. Green, *Macromolecules*, 1999, **32**, 801–807.

27. D. Slep, J. Asselta, M. H. Rafailovich, J. Sokolov, D. A. Winesett, A. P. Smith, H. Ade and S. Anders, *Langmuir*, 2000, **16**, 2369–2375.

28. C. Wang, G. Krausch and M. Geoghegan, *Langmuir*, 2001, **17**, 6269–6274.

29. H. Kang, S.-H. Lee, S. Kim and K. Char, *Macromolecules*, 2003, **36**, 8579–8583.

30. S. Chattopadhyay and J. C. Meredith, *Macromol. Rapid Commun.*, 2004, **25**, 275–279.

31. P. Müller-Buschbaum, O. Wunnicke, M. Stamm, Y.-C. Lin and M. Müller, *Macromolecules*, 2005, **38**, 3406–3413.

32. Y. Li, Y. Yang, F. Yu and L. Dong, *J. Polym. Sci. Part B Polym. Phys.*, 2006, **44**, 9–21.

33. C. Carelli, A. M. Higgins, R. A. L. Jones and M. Sferrazza, *Phys. Rev, E*, 2006, **73**, 061804.

34. R. Paul and A. R. Esker, *Langmuir*, 2006, **22**, 6734–6738.

35. J. P. de Silva, M. Geoghegan, A. M. Higgins, G. Krausch, M.-O. David, and G. Reiter, *Phys. Rev. Lett*., 2007, 98, 267802.

36. L. Xue, B. Hu and Y. Han, *J. Chem. Phys.*, 2008, **129**, 214902.

37. L. Xu, T. Shi and L. An, *J. Chem. Phys.*, 2009, **130**, 184903.

38. S. C. Thickett, A. Harris and C. Neto, *Langmuir*, 2010, 26, 15989–15999.

39. L. Xu, D. Bandyopadhyay, T. Shi, L. An, A. Sharma and S. W. Joo, *Polymer*, 2011, **52**, 4345–4354.

40. L. Xu, A. Sharma and S. W. Joo, *Macromolecules*, 2011, **44**, 9335–9340.

41. L. Xu, D. Bandyopadhyay, A. Sharma and S. W. Joo, *Soft Matter*, 2011, **7**, 8056–8066.

42. L. Xu, A. Sharma and S. W. Joo, *J. Phys. Chem. C*, 2012, **116**, 21615–21621.

43. K. Kostourou, D. Peschka, A. Münch, B. Wagner, S. Herminghaus and R. Seemann, *Chem. Engg. Process*, 2011, **50**, 531–536.

44. A. M. Telford, S. C. Thickett, M. James and C. Neto, *Langmuir*, 2011, **27**, 14207–14217.

45. C. Neto, *Phys. Chem. Chem. Phys.*, 2007, **9**, 149–155.

46. S. C. Thickett, C. Neto and A. T. Harris, *Adv. Mater.*, 2011, **23**, 3718–3722.

47. K. Kargupta and A. Sharma, *Phys. Rev. Lett.*, 2001, **86**, 4536–4539.

48. K. Kargupta and A. Sharma, *Langmuir*, 2002, **18**, 1893–1903.

49. K. Kargupta and A. Sharma, *J. Chem. Phys.*, 2002, **116**, 3042–3051.

50. K. Kargupta, A. Sharma, *Langmuir*, 2003, **19**, 5153–5163.

51. H. G. Braun and E. Meyer, *Thin Solid Films*, 1999, **345**, 222–228.

52. A. Sehgal, V. Ferreiro, J. F. Douglas, E. J. Amis and A. Karim, *Langmuir*, 2002, **18**, 7041–7048.

53. Z. Zhang, Z. Wang, R. Xing, Y. Han, *Polymer*, 2003, **44**, 3737−3743.

54. D. Julthongpiput, W. Zhang, J. F. Douglas, A. Karim, M. J. Fasolka, *Soft Matter*, 2007, **3**, 613−618.

55. W. Li, Y. Nie, J. Zhang, D. Zhu, X. Li, H. Sun, K. Yu and B. Yang, *Macromol. Chem. Phys.*, 2008, **209**, 247−257.

56. A. Sehgal, D. Bandyopadhyay, K. Kargupta, A. Sharma and A. Karim, *Soft Matter*, 2012, **8**, 10394−10402.

57. N. Rhese, C. Wang, M. Hund, M. Geoghegan, R. Magerle and G. Krausch, *Eur. Phys. J. E*, 2001, **4**, 69−76.

58. C. Luo, R. Xing, Z. Zhang, J. Fu and Y. Han, *J. Colloid Interface Sci.*, 2004, **269**, 158−163.

59. C. Luo, R. Xing and Y. Han, *Surf. Sci.*, 2004, **552**, 139–148.

60. M. Geoghegan, C. Wang, N. Rhese, R. Magerle and G. Krausch, *J. Phys.: Condens. Matter*, 2005, **17**, S389−S402.

61. R. Xing, C. Luo, Z. Wang and Y. Han, *Polymer*, 2007, **48**, 3574−3583.

62. K. Khare, M. Brinkmann, B. M. Law, E. L. Gurevich, S. Herminghaus, R. Seemann, *Langmuir*, 2007, **23**, 12138−12141.

63. N. Ferrell and D. Hansford, *Macromol. Rapid Commun.*, 2007, **28**, 966−971.

64. R. Mukherjee, M. Gonuguntla and A. Sharma, *J. Nanosci. Nanotechnol.*, 2007, **7**, 2069−2075.

65. R. Mukherjee, D. Bandyopadhyay and A. Sharma, *Soft Matter*, 2008, **4**, 2086–2097.

66. B. Yoon, H. Acharya, G. Lee, H. C. Kim, J. Huh, and C. Park, *Soft Matter*, 2008, **4**, 1467−1472.

67. S. Roy, K. J. Ansari, S. S. K. Jampa, P. Vutukuri and R. Mukherjee, *ACS Appl. Mater. Interfaces*, 2012, **4**, 1887–1896.

68. S. Roy, R. Mukherjee, *ACS Appl. Mater. Interfaces*, 2012, **4**, 5375−5385.

69. A. M. Higgins and R. A. L. Jones, *Nature*, 2000, **404**, 476−478.

70. N. Bhandaru, P. S. Goohpattader, D. Faruqui, R. Mukherjee and A. Sharma, *Langmuir*, 2015, **31**, 3203−3214.

71. D. Bandyopadhyay, A. Sharma and C. Rastogi, *Langmuir*, 2008, **24**, 14048−14058

72. D. Bandyopadhyay and A. Sharma, *J. Phys. Chem. C*, 2010, **114**, 2237−2247.

73. Y. Ding, D. U. Ahn, Z. Wang and R. Yang, *Soft Matter*, 2010, **6**, 4900−4907.

74. D. U. Ahn and Y. Ding, *Soft Matter*, 2011, **7**, 3794−3800.

75. Z. Zhang, D. U. Ahn and Y. Ding, *Macromolecules*, 2012, **45**, 1972−1981.

76. Z. Zhang, L. Wang and Y. Ding, Langmuir, 2013, **29**, 3073−3079.

77. S. Roy, D. Biswas, N. Salunke, A. Das, P. Vutukuri, R. Singh and R. Mukherjee, *Macromolecules*, 2013, **46**, 935–948.

78. N. Bhandaru, A. Das, N. Salunke and R. Mukherjee, *Nano Lett.*, 2014, **14**, 7009–7016.

79. S. Roy, N. Bhandaru, R. Das, G. Harikrishnan and R. Mukherjee, *ACS Appl. Mater. Interfaces*, 2014, **6**, 6579–6588.

80. R. Mukherjee, M. Gonuguntla and A. Sharma, *J. Nanosci. Nanotechnol.,* 2008, **8**, 3406–3415.

81. R. Mukherjee and A. Sharma, *ACS Appl. Mater. Interfaces*, 2012, **4**, 355–362.

82. C. J. Van Oss, M. K. Chaudhury and R. J. Good, *Chem. Rev.*, 1988, **88**, 927–941.

83. R. Mukherjee and A. Sharma, *Soft Matter*, 2015, **DOI:** 10.1039/C5SM01724F.

TOC:

Dewetting of a Thin Polymer Bilayer on a Cross Patterned Substrate

Route to Novel Meso Patterning